

Massively parallel finite difference elasticity using a block-structured adaptive mesh refinement with a geometric multigrid solver

Brandon Runnels^{a,*}, Vinamra Agrawal^b, Weiqun Zhang^c and Ann Almgren^c

^a*Department of Mechanical & Aerospace Engineering, University of Colorado, Colorado Springs, CO, USA*

^b*Department of Aerospace Engineering, Auburn University, Auburn, AL, USA*

^c*Lawrence Berkeley National Laboratory, Berkeley, CA, USA*

ARTICLE INFO

Keywords:

Numerical methods
Adaptive mesh refinement
Solid mechanics
Finite difference method
Mechanics of materials

ABSTRACT

The finite element method (FEM) is, by far, the dominant method for performing elasticity calculations. The advantages are primarily (1) its ability to handle meshes of complex geometry using isoparametric elements, and (2) the weak formulation which eschews the need for computation of second derivatives. Despite its widespread use, FEM performance is sub-optimal when working with adaptively refined meshes, due to the excess overhead involved in reconstructing stiffness matrices. Furthermore, FEM is no longer advantageous when working with representative volume elements (RVEs) that use regular grids. Block-structured AMR (BSAMR) is a method for adaptive mesh refinement that exhibits good scaling and is well-suited for many problems in materials science. Here, it is shown that the equations of elasticity can be efficiently solved using BSAMR using the finite difference method. The boundary operator method is used to treat different types of boundary conditions, and the "reflux-free" method is introduced to efficiently and easily treat the coarse-fine boundaries that arise in BSAMR. Examples are presented that demonstrate the use of this method in a variety of cases relevant to materials science, including Eshelby inclusions, material discontinuities, and phase field fracture. It is shown that the implementation scales very well to tens of millions of grid points and exhibits good AMR efficiency

1. Background and Motivation

The finite element method (FEM) is ubiquitous in computational science and engineering, particularly for solving elasticity problems [1]. FEM is advantageous because the use of isoparametric elements facilitates the use of complex, geometry-conforming discretizations. This allows computational scientists to create meshes for highly complicated problems without complex stencils or troublesome boundary conditions. Furthermore, FEM is formulated using the weak form. This removes the need for computing second derivatives, which can be an arduous task when working with tensor-valued fields. FEM also lends itself well to the Ritz variational method, simplifying the solution of affine and nonlinear problems. Despite its wide use, there are limitations in FEM that can be solved by looking to other methods. Here, we propose that the use of the Finite Difference Method (FDM) is advantageous for some problems in elasticity, and propose an efficient method of solving the elastic FDM problem using block-structured AMR. We demonstrate the use of FDM in BSAMR, and develop

a new approach for accurately treating the boundary between AMR levels (the "coarse-fine boundary").

The motivating application of interest here is multiscale mechanics of materials. Materials are well-known to exhibit drastically different properties on different scales [2]. Crystalline materials such as metals typically behave isotropically on the macroscale, but exhibit a non-trivial stress pattern at the microscale (even under uniform loading) resulting from their complex grain structure. The sub-grain response, in turn, is determined by the crystalline structure and the existence of defects (such as dislocations) at the atomic scale. Therefore, to obtain material response informed by first-principles calculations, it is necessary to bridge spatial and temporal scales. A common way to link scales is by simulating complex behavior that takes place on the mesoscale within representative volume elements (RVEs). RVE simulations incorporate atomistically-informed physics (such as grain boundary and plasticity models [3, 4, 5]) to provide continuum-level mechanical data (such as elastic moduli or yield stress). RVE simulation domains can exist on scales ranging from nanometers to centimeters (depending on the application), but are common in that the simulation domain is rectilinear and periodic. The features of interest are neither the geometry of the

*Corresponding Author

ORCID(s): 0000-0003-3043-5227 (B. Runnels);
0000-0002-1698-1371 (V. Agrawal)

domain nor the boundary conditions (as is often the case in FEM applications), but rather the material discontinuities within the RVE and the resulting heterogeneous response.

A common example of such RVE simulations is the evolution of microstructure in metals, in which the grain boundaries (GB) move to reduce their energy and the elastic energy of the material. This presents the problem of generating a suitable discretization that adapts to the ever-changing microstructure in the RVE. One way of addressing this problem is through the use of diffuse interface methods such as the multi-phase field (MPF) method for microstructure evolution [6, 7]. In this method, rather than mesh the microstructure explicitly, a uniform grid is used to resolve the transition region between grains. This method is highly advantageous in that it allows for fully arbitrary microstructure evolution and is not hindered by topological transitions such as boundary splitting/merging. However, it can also be computationally expensive due to the excessive number of trivial grid points located within the interior of each grain. To resolve this problem, adaptive mesh refinement (AMR) is used to selectively refine the regions of interest across GBs, while reducing the number of trivial points in the grain interiors. The adaptivity of the method allows the mesh to be freely driven by the evolution of the problem.

Many flavors and varieties of AMR are available [8]. Block-structured AMR (BSAMR) is an AMR method in which the mesh is organized into “levels” such that each level is comprised of grid cells that are all the same size [9]. Each level is treated independently, and then coarse levels are updated with information from fine levels using averaging. BSAMR is highly scalable and is well-suited for massive parallelism, compared to other methods that exhibit a prohibitive amount of communication overhead as the mesh size increases. FEM is, in general, not ideal for BSAMR for a number of reasons (which will be discussed in section 3). While parallel AMR FEM implementations have been implemented [10], scalability is ultimately limited by the choice of AMR that is used. Finite difference, on the other hand, lends itself easily to a BSAMR implementation, and is therefore the method of choice for highly scalable code.

Relatively little work has been done to develop the FDM for elasticity. While there has been some work to solve for stresses and displacements using finite difference with a displacement potential function [11, 12], it has not been applied on a large scale. In this work, we discuss the FDM for finite difference, introduce a

BSAMR implementation, and present several numerical results. This paper is organized in the following way. Section 2 reviews the formulation of elasticity and describes the FDM implementation. Section 3 describes the computational framework (“Alamo”), the block-structured adaptive mesh refinement, and the multigrid solver. Section 4 demonstrates the use of the code applied to several classic elastic problems, as well as massively parallel microstructure simulations. Performance and scaling data are discussed in section 5, and we conclude with conclusions and acknowledgments in section 6.

2. Theory and Computation

In this section we review linear elasticity in the strong form only, and the practical challenges involved in constructing a finite-difference implementation. Next, we discuss block-structured AMR and the geometric multigrid method for solving linear system. Finally, we introduce the “reflux-free” method for treating multi-level solutions at coarse-fine boundaries.

2.1. Finite difference method for elasticity

Let $\Omega \subset \mathbb{R}^d$ be the d -dimensional problem domain with boundary $\partial\Omega$. The subset $\partial_1\Omega \subset \partial\Omega$ is the portion of the boundary subjected to *displacement* boundary conditions (also referred to as Dirichlet or essential BCs.) The subset $\partial_2\Omega \subset \partial\Omega$ is the boundary subjected to *traction* boundary conditions (also referred to as natural BCs.) The subset $\partial_3\Omega \subset \partial\Omega$ is the part of the boundary subjected to Neumann boundary conditions. We note that there is an important distinction between traction ($\partial_2\Omega$) and Neumann ($\partial_3\Omega$) conditions and they are not interchangeable.

The following are the governing equations for static linear elasticity:

$$\frac{\partial}{\partial x_j} \left[\mathbb{C}_{ijkl}(\mathbf{x}) \left(\frac{\partial u_k}{\partial x_l} - \varepsilon_{kl}^0 \right) \right] = -b_i(\mathbf{x}) \quad \forall \mathbf{x} \in \text{int}(\Omega) \quad (1a)$$

$$u_i = u_i^0(\mathbf{x}) \quad \forall \mathbf{x} \in \partial_1\Omega \quad (1b)$$

$$\mathbb{C}_{ijkl}(\mathbf{x}) \left(\frac{\partial u_k}{\partial x_l} - \varepsilon_{kl}^0 \right) n_j(\mathbf{x}) = t_i^0(\mathbf{x}) \quad \forall \mathbf{x} \in \partial_2\Omega \quad (1c)$$

$$\frac{\partial u_i}{\partial x_j} n_j(\mathbf{x}) = \delta u_i^0(\mathbf{x}) \quad \forall \mathbf{x} \in \partial_3\Omega. \quad (1d)$$

The tensor ε^0 is an eigenstrain, representing e.g. plastic slip or thermal strain, and is 0 in the linear elastic case.

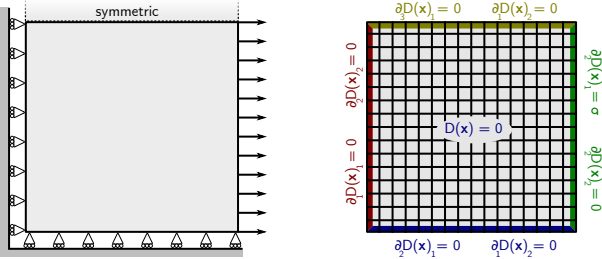


Figure 1: Example of a partitioned boundary operator

\mathbb{C} is the fourth-order, spatially varying elasticity tensor, \mathbf{b} is the body force vector field, and $\mathbf{u}^0, \mathbf{t}^0, \delta\mathbf{u}^0$, are the prescribed displacements, tractions, and displacement gradients, respectively.

In the present finite difference formulation, boundary conditions are treated as boundary operators. Equation 1a is represented by an operator $D : \text{int}(\Omega) \rightarrow \mathbb{R}^d$ acting on displacements, for which the negative body force is the right hand side. Similarly, $\partial_1 D$, $\partial_2 D$, and $\partial_3 D$ are operators acting on displacement vectors in the boundary, for which the right hand sides are prescribed displacement, traction, and displacement gradient, respectively.

Figure 1 illustrates the case of a loaded block with the use of partitioned operators as surrogates for boundary conditions. The partitioned operator is then implemented in such a way that the linear solver can be entirely agnostic to boundary conditions, with boundary condition information passed in as components of the right hand side.

2.1.1. Affine elasticity and material discontinuities

A classic difficulty of the FDM is its inability to treat material discontinuities. For instance, if \mathbb{C}_{ijkl} is discontinuous, then the gradient operation will result in infinity at the discontinuity. The same is true if the eigenstrain $\boldsymbol{\epsilon}^0$ is discontinuous. FEM is not vulnerable to this because the weak formulation replaces the second derivative with two first derivatives. Because FDM computes second derivatives, mesh dependency will inevitably result if the discontinuities are left unchecked.

To remedy this, we simply require that \mathbb{C}_{ijkl} and $\boldsymbol{\epsilon}$ be smooth functions of \mathbf{x} . When the need arises to model a discontinuity, a transition (or “diffuse”) region will be introduced over which the values will be continuously varied. This requires that the mesh be highly refined near the transition region, which is a simple matter with AMR. Indeed, for many applications, other problem constraints already required high resolution at the boundary, so this does not incur any additional

computational cost.

For a problem with spatially varying elastic properties, the operator (1a) is split using the product rule

$$D(\mathbf{u})_i = \mathbb{C}_{ijkl,j}(u_{k,l} - \boldsymbol{\epsilon}_{kl}^0) + \mathbb{C}_{ijkl}(u_{k,l,j} - \boldsymbol{\epsilon}_{kl,j}^0), \quad (2)$$

avoiding the need to create a surrogate stress field. Operator overloading is used extensively to efficiently compute the modulus derivative $\mathbb{C}_{ijkl,j}$ in a portable way. High symmetry tensors (such as those corresponding to isotropic or cubic materials) store only the reduced number of constants, which not only saves space but also significantly speeds up the computation time for the derivative.

For problems with eigenstrain, the operator is decomposed into homogeneous and inhomogeneous components. The homogeneous operator is readily computed to be

$$D_H(\mathbf{u}) = D(\mathbf{u}) - D(\mathbf{0}) \quad (3)$$

Thus the solution to $D(\mathbf{u}) = -\mathbf{b}$ is given simply by the solution to

$$D_H(\mathbf{u}) = -(D(\mathbf{0}) + \mathbf{b}), \quad (4)$$

that is, the inhomogeneous part of the operator is transferred to the right hand side, and acts as a source term in the solution, provided that the eigenstrain field $\boldsymbol{\epsilon}^0$ is C_1 continuous.

3. Implementation

All results were generated using the implementation in Alamo, a C++ code developed by the authors, which is built on the AMReX library. Zhang *et al* [13] is a general reference for this section. For clarity, we define nomenclature in the following table:

3.1. Geometric multigrid solver

Many algorithms for multiphysics PDE-based applications require the iterative solution of large linear systems arising from either discretization of elliptic equations or implicit treatment of parabolic equations. Multigrid algorithms are often the method of choice for solving these systems. AMR simulations with subcycling in time typically require linear solves across the grids at a single AMR level only; algorithms without subcycling typically require solves across all the levels in the hierarchy. For the rest of this paper we focus on the performance of multigrid on multiple levels of an AMR hierarchy, using either V-cycles or F-cycles (see, e.g., [14], for more detail).

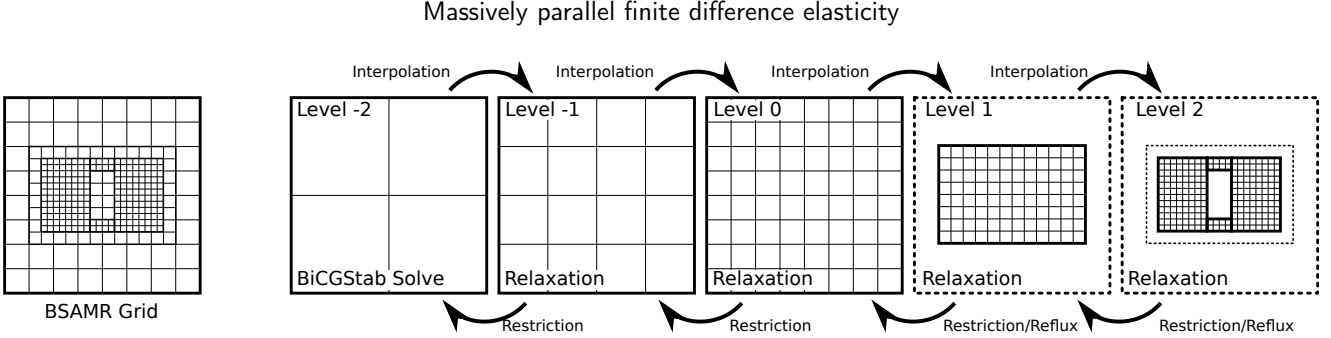


Figure 2: Structure of the multi-level/multi-grid solver, illustrating the continuity between multigrid ($level < 0$) and levels of refinement ($level > 0$).

d	Spatial dimension
i, j, k, l	Indices corresponding to coordinates
m, n	Indices corresponding to “fine” and “coarse” AMR levels
Ω_m	Domain for refinement level m
$\partial\Omega_m^{CF}$	Coarse-fine boundary (not domain boundary)
\mathbf{r}_n	Right hand side on level n
D_n	Linear operator on level n
S_n^D	Relaxation operator on level n
I_{nm}	Interpolation function
R_{mn}	Restriction function

Figure 3: Notation

The multigrid method can be naturally combined with block-structured AMR by viewing the refined levels as an extension of the coarse/fine multigrid level sequence (Figure 2). In this work, we refer to the initial, unrefined grid as “Level 0,” the first level of refinement as “Level 1,” and so on. The first multigrid coarsening level is “Level -1” the second is “Level -2,” etc. A full discussion of multigrid implemented with block-structured AMR is discussed in [15].

In the present work, the multigrid solver is used with F-cycles only. For each smoothing operation, two sequential Jacobi iterations are performed. The solver runs a total of four smoothing operations per level, for a total of eight Jacobi iterations.

Finite element elasticity is not easily amenable to this method. In order for the operator (stiffness matrix) to be consistently refined/coarsened, there must be operator equivalence at each level. The only elements that satisfy this equivalence are bilinear (2D) and trilinear (3D) rectangular elements; however, these are well-known to exhibit shear-locking and other undesirable effects [16]. On the other hand, the finite difference method is easily applied and requires approximately the same number of calculations as FEM.

3.2. Reflux-free BSAMR extension

A main contribution of this work is a novel method for restriction between coarse and fine AMR levels. We proceed in this section by formally defining the necessary properties for relaxation, interpolation, and prolongation. Some of the notation is enumerated in Table 3.

Relaxation The relaxation operator $S_n^D : [C(\Omega_n)]^2 \rightarrow C(\Omega_n)$ is defined such that

$$D_n \left[\lim_{q \rightarrow \infty} (S_n^D)^q(\phi_n) \right] = \mathbf{r}_n \quad \text{on } \text{int}(\Omega_n) \quad (5)$$

that is, the relaxation operator converges to the exact solution with $\partial^{CF} \Omega_m$ acting as part of $\partial_1 \Omega_m$ (Dirichlet boundary).

Interpolation The interpolation operator $I_{nm} : C(\Omega_m \cap \Omega_n) \rightarrow C(\Omega_m)$ projects the solution from the coarse level to the fine level. We require that I_{nm} satisfy the following properties:

1. Translation symmetry: $I_{nm}(\phi \circ t) = I_{nm}(\phi) \circ t$ where $t : \Omega_m \rightarrow \Omega_m$ is an admissible translation operation. This means that the interpolation operator should be the same everywhere in the pre-image of I_{nm} . (Admissible = does not translate outside of pre-image of I_{nm} .)
2. Injectivity: in the special case of BSAMR refinement, level m has higher resolution than level n .

Restriction The restriction operator $R_{mn} : C(\text{int } \Omega_m) \rightarrow C(\text{int } \Omega_m \cap \Omega_n)$ projects the solution from the fine level to the coarse level. R_{mn} must satisfy the following properties

1. Translation symmetry: complementary to interpolation operator.
2. Surjectivity: in the special case of BSAMR refinement, level n has lower resolution than level m .

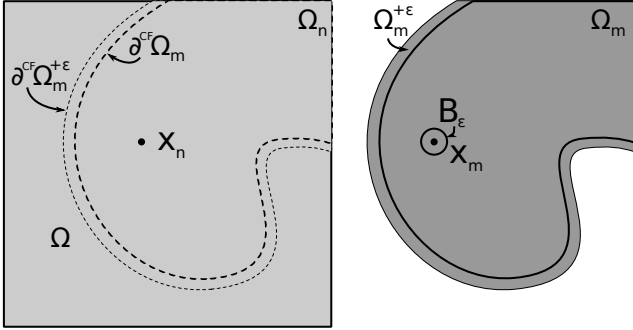


Figure 4: The fine level (Ω_m) must be grown by ϵ in order for the restriction operation to maintain translation symmetry.

3. Nonlocality: $(R_{mn} \circ \phi^n)^{-1}(x_n) = B_\epsilon(x_m)$ where B_ϵ is an ϵ -neighborhood of x_m . That is, the value of the restricted function at the coarse point x_n requires information at *and around* fine-level point x_m .

We see that together, properties of translation symmetry and nonlocality require additional restrictions be placed on the domain of R_{mn} . Consider a point $x_m \in \partial^{CF}\Omega_m$: nonlocality requires dependence on $B_\epsilon(x)$; therefore, this becomes boundary-dependent. To preserve translation symmetry, we make the domain of the restriction operator $\text{dom}(R_{mn}) = C(\text{int}_\epsilon\Omega_m)$, where the “ ϵ -interior” is

$$\text{int}_\epsilon\Omega_m = \{x_m \in \Omega_m : B_\epsilon(x_m) \subset \Omega_m\}. \quad (6)$$

We are now left with the problem of restricting points on the coarse/fine boundary $\partial^{CF}(\Omega_m)$. Improper treatment of coarse/fine boundary can result in mismatched operator, leading to artificial forces and poor convergence. One possibility is to augment the restriction operation with a special operator with mixed stencil that uses information about D to both smooth and restrict ϕ_m . This was proposed by Almgren *et al* [15] as a “reflux” operation, and has been demonstrated to work successfully in many applications [17, 18, 19, 20, 21]. However, when the linear operator D is complicated, the practical implementation of such a reflux operation may become prohibitively difficult to implement. Furthermore, it lacks generality as it requires operator-specific information for restriction.

We propose an alternative modification. Let us define the ϵ -neighborhood of Ω_m (Figure 4)

$$\Omega_m^{+ε} = \{x : \exists x_m \in \Omega_m \text{ such that } x \in B_\epsilon(x_m)\}. \quad (7)$$

Then the pre-image of $R_{mn} \circ \phi_n$ is exactly $\text{int}(\Omega_m^{+ε})$. Numerically, the interpolation operator is implemented as

a basic bilinear (2D) or trilinear (3D) interpolation from the coarse level to the fine level. A standard restriction matrix (with powers of 2) is used for the restriction operator. If the restriction operator acts on each of the N -nearest neighbors, then the fine AMR level is grown to include exactly $N + 1$ “ghost nodes” (corresponding to the discretized $\partial^{+ε}\Omega$). (In general, $N = 1$ for all cases considered here.) A detailed description of the resulting effective stencil is worked out in Appendix A

In a numerical multigrid scheme, the reflux-free method works in the interpolation-smooth-restriction cycle in the following way: For each cycle, the interpolation operator updates all non-boundary fine level nodes with updated values from the coarse level. The fine level is then relaxed, with the outer layer of ghost nodes acting as a Dirichlet boundary with values set by the coarse level. However, all other nodes have been properly updated, including those nodes on the coarse/fine boundary. Therefore, when the solution is restricted from the fine level to the coarse, the pre-image of the restriction operator on the coarse grid is the entirely updated solution. This implementation also preserves the necessary properties of translational symmetry and nonlocality of restriction operator. Finally, this eliminates the need for special treatment, such as a mixed stencil or operator dependent reflux operation, on the coarse/fine boundary. Since ∂_m^{CF} is, by definition, on the interior of the domain, the ϵ -neighborhood is then filled using the interpolation operator.

4. Examples

In this section we present a collection of numerical examples that show the versatility of the method, provide verification against known solutions, and demonstrate scalability and performance. Each section provides brief background on the methods involved in the calculation, but in each case, the literature should be consulted for a full discussion.

4.1. Eshelby inclusion

The Eshelby inclusion for an ellipsoid is a standard problem in linear elasticity that was originally introduced (and solved) by Eshelby [22]. The problem is generally described as follows: consider an ellipsoidal region in a homogeneous, infinite, stress-free solid. Let the ellipsoid be removed from the solid and replaced by an ellipsoid that has been permanently deformed by a strain $\epsilon^{eshelby}$, called an *eigenstrain*. Once the body is allowed to relax, the mismatch induces a residual strain in both the inclusion and the matrix.

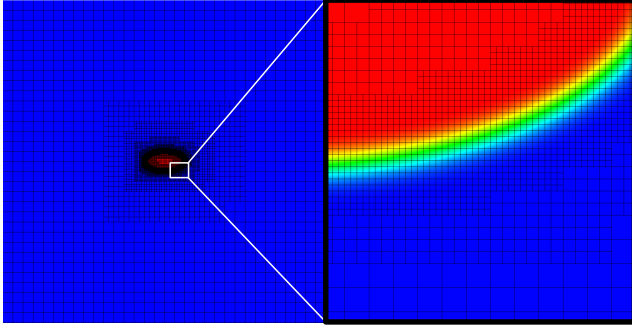


Figure 5: (Eshelby inclusion) Slice of 3D grid with 6 total AMR levels. Blue (exterior) indicates $\epsilon^0 = \mathbf{0}$; red (interior) indicates $\epsilon = \epsilon^{eshelby}$.

Eshelby introduced an analytical solution for this problem and derived the “Eshelby tensor” for the ellipsoidal inclusion [23]. However it was not until recently that the displacement field (and subsequent strain and stress fields) for an arbitrary ellipsoidal inclusion was derived [24]. This ellipsoid inclusion problem is a useful test case for the present elasticity model, as it enables verification of the use of diffuse material discontinuities as well as far-field stresses.

The problem is constructed in a $8 \times 8 \times 8$ (arbitrary length units) domain with fixed-displacement boundary conditions. The large domain approximates the “infinite body” used in the classic Eshelby problem. The base-level grid is 32^3 , and there are 5 levels of refinement for 6 total AMR levels (Figure 5). The width of the diffuse boundary is 0.1 to ensure adequate grid coverage. The radii for the ellipse in the x_1, x_2, x_3 directions are $a_1 = 1.0, a_2 = 0.75, a_3 = 0.5$, the elastic moduli are $E = 210, \nu = 0.3$, and the eigenstrain is $\epsilon^{eshelby} = \text{diag}(1E - 3, 1E - 3, 1E - 3)$ and zero elsewhere. (All values taken from [24].)

The sharp-boundary ellipsoid is determined by the indicator function

$$\eta(\mathbf{x}) = \begin{cases} 1 & \mathbf{x}^T \mathbf{A} \mathbf{x} > 1 \\ 0 & \text{else} \end{cases}, \quad (8)$$

(with $\mathbf{A}_{ij} = (\epsilon_{ij}^{eshelby})^{-2}$). The diffuse indicator function η_ϵ is constructed in the following way:

$$\eta_\epsilon(\mathbf{x}) = \frac{1}{2} \left(1 - \text{erf} \left(\frac{\mathbf{x}^T \mathbf{A} \mathbf{x}}{2 \epsilon |\mathbf{A} \mathbf{x}|} \right) \right). \quad (9)$$

Since $2 \mathbf{A} \mathbf{x}$ is the slope of η , dividing the argument of the error function by the magnitude of its slope ensures a generally uniform diffuse region. The eigenstrain field is then given by

$$\epsilon(\mathbf{x}) = \eta(\mathbf{x}) \epsilon^{eshelby}. \quad (10)$$

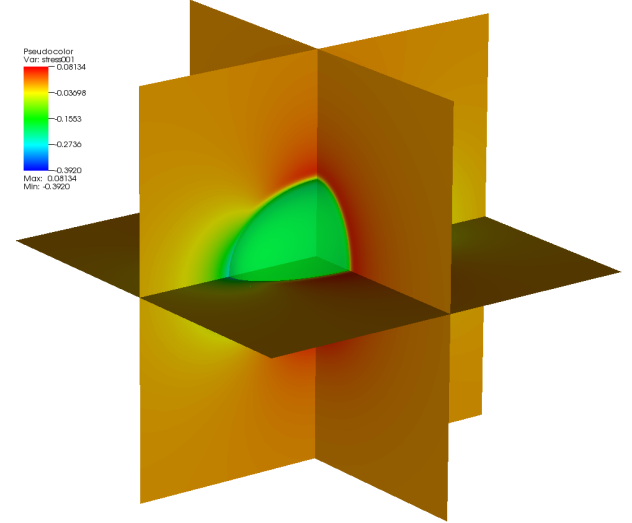


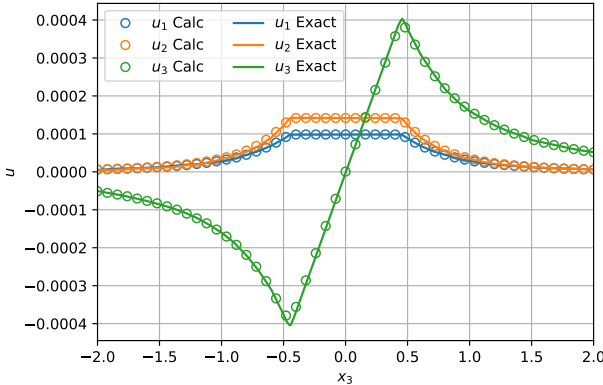
Figure 6: (Eshelby inclusion) Slice plot of σ_{33} (green ellipse indicates the boundary of the inclusion)

To solve the problem, an AMR mesh is used with a total of 1,010,240 grid points, and the finest level consists of 667,712 nodes concentrated over 0.062% of the domain volume. As the focus of this test was validation, the parameters of the numerical solution are not optimized for performance; for instance, it does not take advantage of symmetry. However, the MLMG solver completed in approximately 2 minutes on a laptop running with 6 MPI processes. The convergence factor was 0.1 for the first few iterations before reaching a constant factor of 0.5 after 2-3 iterations.

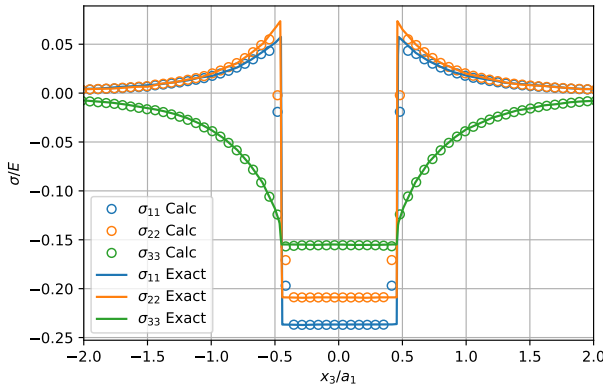
Stresses and displacements are determined for the entire region (Figure 6). It is determined that all displacements, strains, and stresses drop off to zero at a substantial distance from the domain boundary.

To validate the solution, displacements, strains, and stresses are compared to exact values in Jin *et al* [24]. The values are determined along the line between the points $[0.25, 0.25, -4]$ and $[0.25, 0.25, 4]$. Comparison is included here for displacements (Figure 7a) and normal stresses (Figure 7b).

The match is nearly exact in all cases for displacements, normal/shear strain, and normal/shear stress. The only region with a substantial difference is at $x_3 = \pm -0.5$, which is the location of the diffuse boundary. The stress is shown to be discontinuous, but the diffuse boundary smooths out the discontinuity and allows the stress to vary smoothly between the interior and exterior of the inclusion. There is no apparent effect on the solution away from the diffuse boundary.



(a) Displacements vs analytical solution



(b) Stresses vs. analytical solution

Figure 7: (Eshelby inclusion) Comparison of displacements and normal stresses to analytical solution as derived in [24]

4.2. Fracture

Catastrophic and incremental failure in solid materials is often mediated by the nucleation and propagation of fractures. Crack propagation in brittle and ductile materials has been a topic of study for decades. With recent advancements in additive manufacturing methods, modeling fatigue-induced crack propagation in additively manufactured metals is particularly important [25].

One of the many prominent techniques of modeling fracture is the cohesive zone modeling. This technique involves defining a traction-separation relationship across fracture surfaces [26]. Some cohesive zone models introduce potential functions to define the non-linear traction-separation relationship. Cohesive zone models have been successfully used to capture effects of crack tip radius and plasticity effects near the crack tip [27]. However, implementation of the cohesive zone model requires interface elements to be placed along the path of fracture. This requires anticipating the crack path, and could potentially lead to mesh dependency

[28].

Phase field fracture (PFF) methods are another class of techniques that replace a sharp crack with a diffused crack field $\eta(\mathbf{x}, t)$ with an associated length scale η_ϵ [29, 30, 31]. The crack field is set to 1 inside the crack, and zero outside. PFF methods introduce an energy contribution corresponding to the crack field which governs crack field evolution. Additionally, a regularization term is introduced that circumvents the mesh dependency of the solution. The PFF solution has been mathematically shown to converge to the analytical linear elastic fracture mechanics (LEFM) solution in the limit $\eta_\epsilon \rightarrow 0$ [30].

Central to all of these methods is the computation of a stress field around a crack tip, which always produces highly localized strain fields. In each of these cases, the mesh must be highly refined near the crack tip but can be coarse in the far field. In some cases this is accomplished by completely re-meshing at various intervals or by pre-meshing in anticipation of the crack's path [32, 33, 34]. Here, we apply the finite difference BSAMR linear solver to the problem of linear elastic fracture mechanics for use with PFF.

The energy functional \mathcal{F} is written as

$$\mathcal{F} = \int_{\Omega} g(\eta) W(\nabla \mathbf{u}) d\Omega + \int_{\Omega} \mathcal{G}_c \left[\frac{w(\eta)}{\eta_\epsilon} + \eta_\epsilon |\nabla \eta|^2 \right] d\Omega \quad (11)$$

where \mathcal{G}_c is the crack fracture energy, \mathbf{u} is the displacement, $W(\nabla \mathbf{u}) = \mathbb{C}_{ijkl} u_{i,j} u_{k,l}$ is the elastic strain energy and η_ϵ is the length scale associated with diffused crack width. Additionally, the functions $g(\eta)$ and $w(\eta)$ are differentiable functions chosen such that $g(\eta = 1) = 1$ and $w(\eta = 1) = 0$. In this case, $g(\eta) = \eta^2$ and $w(\eta) = 1 - g(\eta)$. The last term in equation (11) is for crack regularization that eliminates mesh dependency of the solution.

The equilibrium equations for \mathbf{u} and η are obtained using the variational derivative of \mathcal{F} with \mathbf{u} and η respectively. It can be shown that the stress equilibrium equation is

$$\operatorname{div} \left(g(\eta) \frac{\partial W}{\partial (\nabla \mathbf{u})} \right) = 0 \quad (12)$$

A two dimensional rectangular domain $(-4, -4) \times (4, 4)$ is chosen with a notch of length a , thickness t and semi-circular ends of radius $t/2$, centered at $(0, 0)$. The boundary is mollified with length scale ϵ using the error function approach described in equation (9). To solve the problem, a base mesh of 512×512 points was chosen with 5 levels of refinement. The elastic modulus was

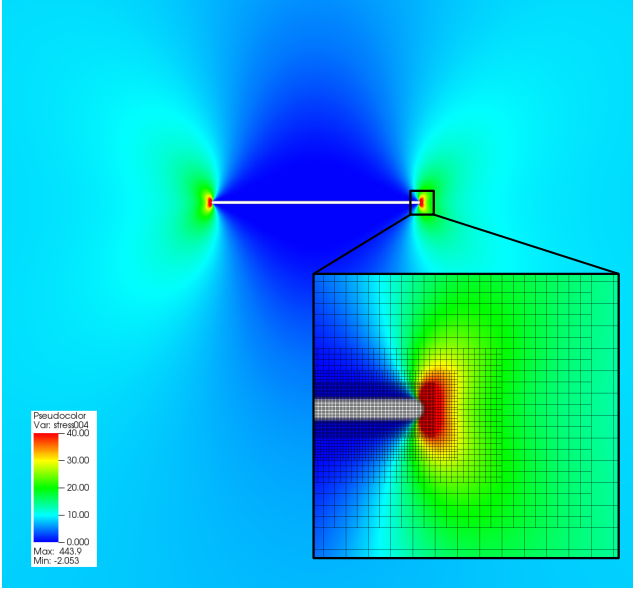


Figure 8: (Fracture) Far field stress (σ_{22}) field (main) and detail of stress field near crack tip (inset).

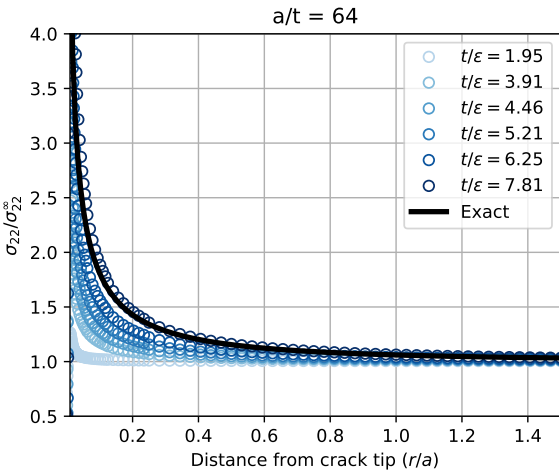


Figure 9: (Fracture) Variation of crack stress σ_{22} with r at $\theta = 0$, for fixed crack length to thickness ratio and different mollification length scales. The analytical solution is compared to the data.

capped to 1% inside the crack to maintain numerical stability. Computations were performed with MPI using 16 cores. The stress distribution near the crack tip is shown in Figure 8.

To validate the BSAMR approach, stress σ_{22} is plotted along $y = 0$ line for $a/t = 64$ and different mollification length scales. The results are compared to analytical LEFM solutions provided in [35, 36] in Figure 9. It can be observed that as mollification length scale reduces, the predicted crack stresses approach the analytical solution (Figure 9).

4.3. Phase field microstructure

A primary motivational application of interest for the present work is RVE mesoscale simulations of microstructural response. The multiphase field (MPF) method is used to evolve boundaries. Though the MPF method itself is a focus of this work, we present a brief overview here. Let a polycrystal with N grains be represented by N order functions called order parameters $\{\eta_1, \dots, \eta_N\} \subset C(\Omega, [0, 1])$. The order parameters act as indicator functions for the regions occupied for each grain; grain n occupies the region in which $\eta_n = 1$. The boundaries are diffuse, such that there is a smooth transition region between grain with a characteristic length ℓ (Figure 10). The order parameters are evolved using the differential equations

$$\frac{\partial \eta^n}{\partial t} = -L \frac{\delta F}{\delta t} \quad (13)$$

where $F(\eta_1 \dots \eta_N, \nabla \eta_1 \dots \nabla \eta_N)$ is a free energy functional. For more details on the method see [37, 38, 39, 40].

An example of an implementation using the base form of F is discussed in [40], although we do not consider the higher-order regularization here. To account for mechanically-driven grain boundary motion, the functional F also contains an elastic energy term:

$$\frac{1}{2} \boldsymbol{\varepsilon} : \mathbb{C}(\eta_1, \dots, \eta_N) : \boldsymbol{\varepsilon}, \quad (14)$$

where $\boldsymbol{\varepsilon}$ are the solutions to the linear elasticity problem and the elastic modulus tensor \mathbb{C} is given by a simple mixture rule

$$\mathbb{C}(\eta_1, \dots, \eta_N) = \sum_{i=1}^N \mathbb{C}_i \eta_i. \quad (15)$$

Other mixture rules can be used (c.f. [38]), but a linear rule is sufficient for purposes of model demonstration.

The unrotated fourth order elastic modulus tensor is expressed in Voigt notation as

$$\mathbb{C} = \begin{bmatrix} C_{11} & C_{12} & C_{12} & 0 & 0 & 0 \\ C_{12} & C_{11} & C_{12} & 0 & 0 & 0 \\ C_{12} & C_{12} & C_{11} & 0 & 0 & 0 \\ 0 & 0 & 0 & C_{44} & 0 & 0 \\ 0 & 0 & 0 & 0 & C_{44} & 0 \\ 0 & 0 & 0 & 0 & 0 & C_{44} \end{bmatrix} \quad (16)$$

which solves $\boldsymbol{\sigma} = \mathbb{C} \boldsymbol{\varepsilon}$ when

$$\boldsymbol{\sigma} = [\sigma_{11} \ \sigma_{22} \ \sigma_{33} \ \sigma_{23} \ \sigma_{31} \ \sigma_{12}]^T, \text{ and} \quad (17)$$

$$\boldsymbol{\varepsilon} = [\varepsilon_{11} \ \varepsilon_{22} \ \varepsilon_{33} \ 2\varepsilon_{23} \ 2\varepsilon_{31} \ 2\varepsilon_{12}]^T. \quad (18)$$

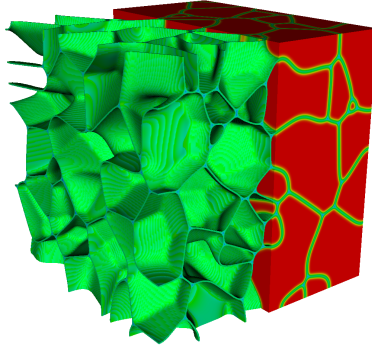


Figure 10: (Microstructure) Plot of $\sum_i \eta_i \eta_i$ highlighting boundary regions - isosurfaces (left) and full field (right)

Each crystal is given a random orientation $\mathbf{R} \in SO(3)$, and the rotated elastic modulus tensor $\hat{\mathbb{C}}$ is

$$\hat{\mathbb{C}}_{pqst} = R_{pi} R_{qj} \mathbb{C}_{ijkl} R_{ks}^T R_{lt}^T. \quad (19)$$

To retain all crystallographic information, it is necessary to retain, at minimum, 6 constants: the moduli C_{11}, C_{12}, C_{44} , and the 3 degrees of freedom associated with the rotation. However, storing only these constants would require an extensive number of trigonometric calculations every time the stress is calculated, which would be computationally intensive. Instead, all 21 components (the symmetric part of \mathbb{C}) are stored at each point.

To set up the simulation, a cubic RVE is used and initialized using a Voronoi tessellation. For all simulations, a total of 10 order parameters are used; however, the order parameters are re-used, and the Voronoi tessellation initializes up to 400 grains. Each order parameter is initialized with a randomly selected orientation. The evolution equation (13) is integrated for 10 timesteps, which allows the grain boundaries to sufficiently diffuse. This is necessary in order to avoid mesh-size dependent effects resulting from aliasing at the grain boundaries.

For the phase field evolution, the following parameters are used. Grain boundary mobility is $M = 1.0$, and the constants for the chemical potential are $\mu = 10.0, \gamma = 1.0$. The diffuse grain boundary width is $\ell_{GB} = 0.025$ to ensure sufficient resolution. The grain boundary energy is $\sigma_0 = 0.075$. The three cubic elastic constants are $C_{11} = 1.68, C_{12} = 1.21, C_{44} = 0.75$. The spatial dimension for the simulation domain are $\Omega = [0, 10]^3 / [0, 5]^3$. A base grid (refinement level 0) is 64^3 (large) and 32^3 (small). For the large simulations, 400 grains were used, for the small, 10 grains. In all cases, 4 AMR levels are used. For the multigrid solver, 6 levels were used for the large grid and 5 for the small.

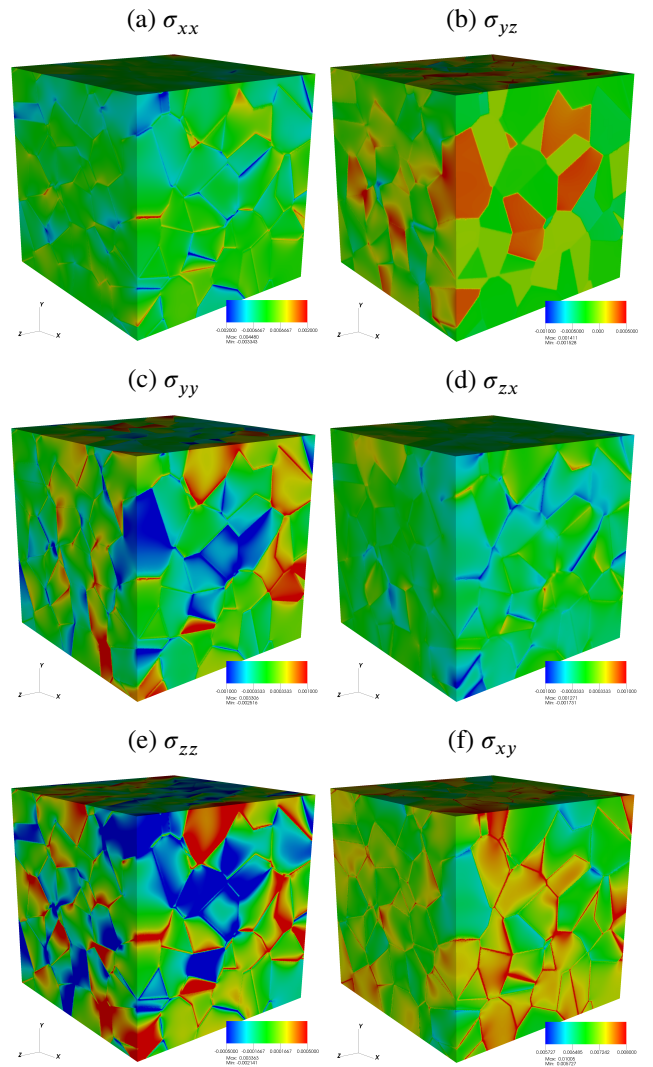


Figure 11: (Microstructure) Plot of components of σ

Once the boundaries have evolved and diffused, a mechanical loading boundary condition is applied. The top is subjected to a shear displacement of 0.1, and the displacement field is relaxed using the AMR multi-level multi-grid solver.

The solution is a complex stress field resulting from the crystallographic anisotropy and heterogeneity resulting from the polycrystalline structure. The six stress components (normal stresses $\sigma_{xx}, \sigma_{yy}, \sigma_{zz}$, shear stresses $\sigma_{yz}, \sigma_{zx}, \sigma_{xy}$) are plotted in Figure 11. A full analysis of these results is outside the scope of this work, but they are consistent with experimental observation. The von-Mises stress is defined as

$$\sigma_{VM} = \sqrt{\frac{3}{2} S_{ij} S_{ij}}, \quad (20)$$

where S_{ij} is the stress deviator tensor. σ_{VM} is plotted in

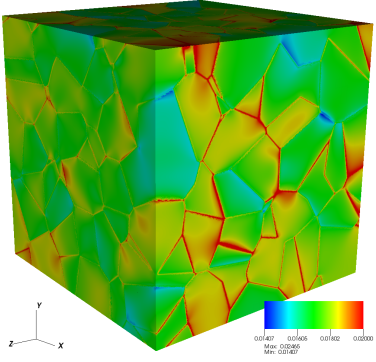


Figure 12: (Microstructure) Von Mises stress

Figure 12, and indicates (unsurprisingly) that the maximum von Mises stress occurs at the grain boundaries.

The solver generally converges in no more than 36 iterations, and this number remained constant regardless of problem size or scaling. Similar tests have been run for isotropic materials (in which the isotropic constants, rather than the crystallographic orientation, varies between grains) and the solver consistently converges in about half the number of iterations. This difference is most likely due to the inefficacy of the Jacobi preconditioner on cubic materials compared to isotropic; more optimal preconditioners can be used for further performance enhancement. The microstructure calculations were used as a benchmark for performance, which is discussed in detail in the following section.

5. Performance

The Alamo implementation of the finite difference reflux-free AMR method was tested for BSAMR efficiency and massive parallelism. In all of the tests presented here, only the time spent in the linear solver is reported. The time spent initializing the Voronoi microstructure, and the time required to evolve the phase field order parameters, are not included in the performance analysis.

5.1. AMR performance

2D tests are run on the phase field microstructure and Eshelby inclusion problems to determine the effect of AMR on the solver efficiency. All tests are run on a laptop using no more than 6 MPI processes.

For each case, a simulation is performed at maximum resolution for the entire domain, with no AMR. As additional AMR levels are added, the maximum resolution remains the same, so that the final results are identical in accuracy. Figure 13 illustrates this process

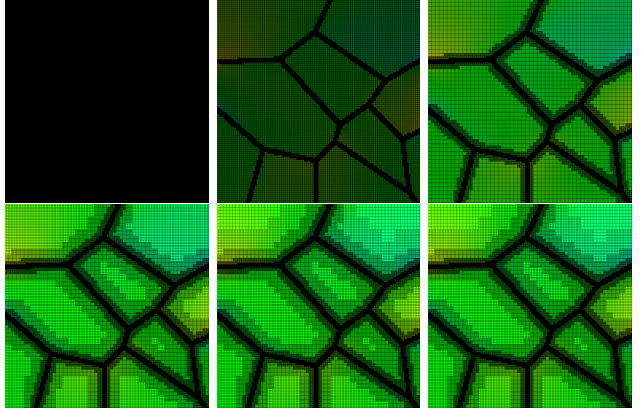


Figure 13: Meshes with varying levels of refinement, beginning with no refinement (upper left).

for phase field microstructure, applying up to 5 levels of AMR. It can be seen that there is initially a dramatic decrease in the number of nodes for the first 2-3 AMR applications; however, there is no difference between the 5-level case and the 4-level case as it is not possible to re-grid without violating the AMR conditions. We refer to the point at which additional AMR levels are not beneficial as “AMR saturation.”

For the phase field microstructure case, AMR saturation is reached at 2-3 refinement levels. For the Eshelby inclusion case, it is reached at 4-5. This is nothing other than a function of the geometry of the problem, the optimization of which is outside the scope of this paper.

Solver data is collected for each of these simulations at each level of refinement (Figure 14) For the Eshelby case, the processing time scaled nearly perfectly with the number of nodes, for a maximum speedup of approximately 6,600%. This can be attributed to the extreme well-suitedness of the Eshelby problem to AMR: the region of interest is extremely small compared to the domain size, and is confined to a nearly spherical region.

The phase field microstructure results similarly indicate that the solver performance scales similarly with the node count, although the scaling is not nearly as close as that for the Eshelby case, only achieving a speedup of about 230%. This is to be expected, as the refined region for the microstructure case is non-localized, resulting in a large amount of coarse/fine interface.

5.2. Parallel scaling

Large and small-scale strong scaling tests were performed using the STAMPEDE2 supercomputer at the Texas Advanced Computing Center. STAMPEDE has 1,736 compute nodes with Intel Xeon Platinum 8160 (“Skylake”) nodes; each has two sockets with 24 cores per socket.

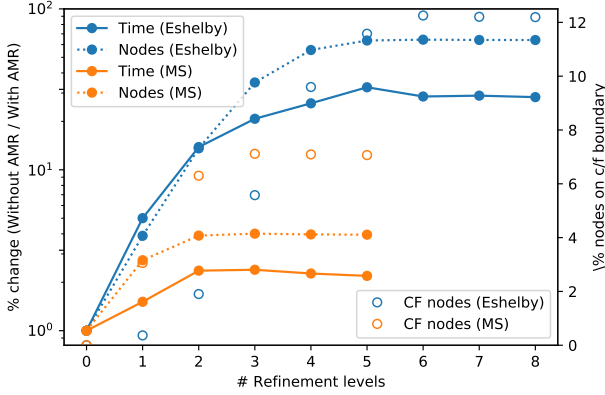


Figure 14: Performance data for Eshelby (blue) and Microstructure (gold) cases. Solid lines represent the no-AMR solver time divided by the AMR solver time; dashed lines represent the number of nodes on the fully-refined grid divided by the number of nodes on the AMR grid. Unfilled markers indicate the percentage of the computational domain on the coarse/fine boundary.

For small-scale, single-node scaling tests, the small microstructure parameters were used. Speedup results are shown in Figure 15. For 1-16 processors, nearly perfect speedup is observed. This is unsurprising as the number of MPI processes is less than the number of cores per socket, and so the entire computation is on a single socket. Once the number of processors exceeds 24, there is a dip in performance below ideal speedup due to the overhead resulting from inter-node communication. Nevertheless, speedup continues to increase at nearly the same rate. The minimum computation time for the solver with 48 MPI tasks was approximately 8.3 minutes with 7,640,576 total grid points distributed among 4 AMR levels. On the finest AMR level, 5,588,480 nodes were concentrated on 33% of the simulation domain. (Note: time for initialization, phase field evolution, and plot file I/O is not included here.)

Small-scale single-node scaling tests are repeated on a small workstation using AMD EPYC CPUs (Figure 15). The simulation involves 10 grains, with four AMR levels subject to an elastic loading. The workstation used has 2x AMD EPYC 7282 processors (16 core/32 thread), with 64 GB RAM. It is observed that the performance drops when simulation is run for all 64 threads. This performance decrease is attributed to machine overhead effects that come into picture when 100% of the machine is being used.

For large-scale, multi-node scaling tests, the large microstructure parameters are used. Relative speedup results (i.e. speedup based on the smallest number of

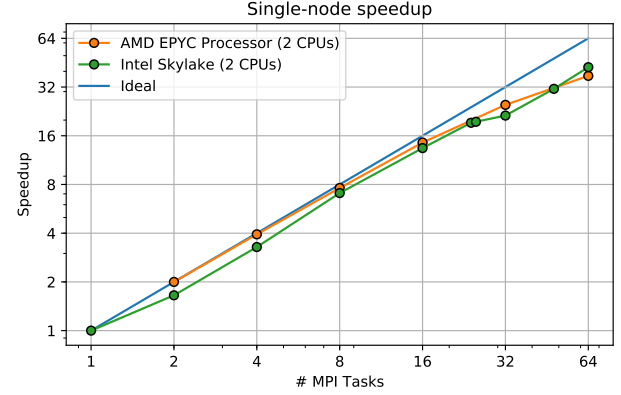


Figure 15: Speedup measurements with 10 grains, 7.6 million grid points on Intel Skylake processors (green) and AMD EPYC processors.

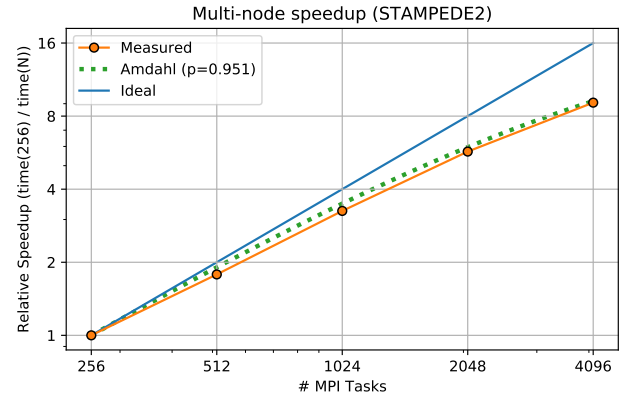


Figure 16: Relative speedup measurements with 400 grains, 102.1 million grid points, on the STAMPEDE2 supercomputer. (Relative speedup = time with N processors / time with 256 processors)

MPI tasks) are plotted in Figure 16. Amdahl's speedup curve is included as well, with an experimentally measured value of $p = 0.951$.

6. Conclusions and Acknowledgments

In this work we have developed and tested a finite difference elastic solver on block-structured AMR grids with geometric multigrid. While FEA is a mainstay of computational solid mechanics, BSAMR is an application in which the traditional advantages of FEM are no longer applicable. For computational problems that use BSAMR, the proposed method has shown to be a feasible alternative. Verification was provided by comparison to the standard Eshelby inclusion case, as well as the fracture mechanics case. It was shown that the method is capable of resolving a stress field around an approximated void with a diffuse boundary. Finally,

the method was applied to large microstructure evolution problems, and shown to produce reasonable results. More importantly, the method was shown to exhibit good scaling, making it a feasible method for computational micromechanics.

There are some limitations to the proposed method. First, it is limited to meshes composed only of regular grids. Second, it requires all material discontinuities to be diffused in order to avoid a singularity resulting from the second derivative. Therefore, the primary domain of application of this method is those cases in which these requirements are already satisfied.

BR acknowledges support from Lawrence Berkeley National Laboratory (LBL) subcontract #7473053, as well as some support from the UCCS Committee for Research and Creative Works. VA acknowledges Hopper computing cluster at Auburn University. WQ and AA acknowledge support from the U.S. Department of Energy, Office of Science, Office of Advanced Scientific Computing Research, Applied Mathematics Program under Award No. DE-SC0008271 and under Contract No. DE-AC02-05CH11231. The HPC parts of this work were made possible through the use of the STAMPEDE2 supercomputer at the Texas Advanced Computing Center (TACC), through an allocation provided by the Extreme Science and Engineering Discovery Environment (XSEDE) [41], allocation # TG-PHY130007. XSEDE is supported by National Science Foundation grant number ACI-1548562.

References

- [1] J. Reddy, *Introduction to the Finite Element Method*. McGraw-Hill Education, 4 ed., 2018.
- [2] M. A. Meyers, *Dynamic behavior of materials*. John wiley & sons, 1994.
- [3] S. Keshavarz and S. Ghosh, “Multi-scale crystal plasticity finite element model approach to modeling nickel-based superalloys,” *Acta Materialia*, vol. 61, no. 17, pp. 6549–6561, 2013.
- [4] S. Keshavarz and S. Ghosh, “Hierarchical crystal plasticity fe model for nickel-based superalloys: sub-grain microstructures to polycrystalline aggregates,” *International Journal of Solids and Structures*, vol. 55, pp. 17–31, 2015.
- [5] M. Jafari, M. Jamshidian, S. Ziae-Rad, D. Raabe, and F. Roters, “Constitutive modeling of strain induced grain boundary migration via coupling crystal plasticity and phase-field methods,” *International Journal of Plasticity*, vol. 99, pp. 19–42, 2017.
- [6] S. Vedantam and B. Patnaik, “Efficient numerical algorithm for multi-phase field simulations,” *Physical Review E*, vol. 73, no. 1, p. 016703, 2006.
- [7] G. Schmitz, B. Böttger, J. Eiken, M. Apel, A. Viardin, A. Carré, and G. Laschet, “Phase-field based simulation of microstructure evolution in technical alloy grades,” *International Journal of Advances in Engineering Sciences and Applied Mathematics*, vol. 2, no. 4, pp. 126–139, 2010.
- [8] T. Plewa, T. Linde, and V. G. Weirs, “Adaptive mesh refinement-theory and applications,” *Lecture notes in computational science and engineering*, vol. 41, pp. 3–5, 2005.
- [9] A. Dubey, A. Almgren, J. Bell, M. Berzins, S. Brandt, G. Bryan, P. Colella, D. Graves, M. Lijewski, F. Löffler, *et al.*, “A survey of high level frameworks in block-structured adaptive mesh refinement packages,” *Journal of Parallel and Distributed Computing*, vol. 74, no. 12, pp. 3217–3227, 2014.
- [10] E. Neiva, S. Badia, A. F. Martín, and M. Chiumenti, “A scalable parallel finite element framework for growing geometries. application to metal additive manufacturing,” *International Journal for Numerical Methods in Engineering*, vol. 119, no. 11, pp. 1098–1125, 2019.
- [11] J. Morales, J. Moreno, and F. Alhama, “Numerical solution of 2d elastostatic problems formulated by potential functions,” *Applied Mathematical Modelling*, vol. 37, no. 9, pp. 6339–6353, 2013.
- [12] K. Harangus and A. Kakucs, “Finite-difference solution using displacement potential function for plane stresses and displacements,” *Procedia Technology*, vol. 12, pp. 394–400, 2014.
- [13] W. Zhang, A. Almgren, V. Beckner, J. Bell, J. Blaschke, C. Chan, M. Day, B. Friesen, K. Gott, D. Graves, *et al.*, “Amrex: a framework for block-structured adaptive mesh refinement,” *Journal of Open Source Software*, 2019.
- [14] W. L. Briggs, S. F. McCormick, *et al.*, *A multigrid tutorial*, vol. 72. Siam, 2000.
- [15] A. S. Almgren, J. B. Bell, P. Colella, L. H. Howell, and M. L. Welcome, “A conservative adaptive projection method for the variable density incompressible navier-stokes equations,” *Journal of computational Physics*, vol. 142, no. 1, pp. 1–46, 1998.
- [16] H. Stolarski and T. Belytschko, “Shear and membrane locking in curved c0 elements,” *Computer methods in applied mechanics and engineering*, vol. 41, no. 3, pp. 279–296, 1983.
- [17] K. Sverdrup, N. Nikiforakis, and A. Almgren, “Highly parallelisable simulations of time-dependent viscoplastic fluid flow simulations with structured adaptive mesh refinement,” *arXiv preprint arXiv:1803.00417*, 2018.
- [18] J. Ream, M. Henry de Frahan, M. Martin, S. Yellapantula, and R. W. Grout, “Numerical simulations of the supercritical carbon dioxide round turbulent jet,” tech. rep., National Renewable Energy Lab.(NREL), Golden, CO (United States), 2019.
- [19] J.-L. Vay, A. Almgren, J. Bell, L. Ge, D. Grote, M. Hogan, O. Kononenko, R. Lehe, A. Myers, C. Ng, *et al.*, “Warp-x: A new exascale computing platform for beam-plasma simulations,” *Nuclear Instruments and Methods in Physics Research Section A: Accelerators, Spectrometers, Detectors and Associated Equipment*, vol. 909, pp. 476–479, 2018.
- [20] A. J. Nonaka, “The amrex block structured adaptive mesh refinement library: Astrophysical applications,” in *American Astronomical Society Meeting Abstracts# 233*, vol. 233, 2019.
- [21] W. D. Fullmer, A. S. Almgren, M. Rosso, J. Blaschke, and J. Musser, “Benchmarking of a preliminary mfix-exa code,” *arXiv preprint arXiv:1909.02067*, 2019.
- [22] J. D. Eshelby, “The determination of the elastic field of an ellipsoidal inclusion, and related problems,” *Proceedings of the Royal Society of London. Series A. Mathematical and Physical Sciences*, vol. 241, no. 1226, pp. 376–396, 1957.
- [23] J. D. Eshelby, “The elastic field outside an ellipsoidal inclusion,” *Proceedings of the Royal Society of London. Series A. Mathematical and Physical Sciences*, vol. 252, no. 1271, pp. 561–569, 1959.
- [24] X. Jin, D. Lyu, X. Zhang, Q. Zhou, Q. Wang, and L. M. Keer, “Explicit analytical solutions for a complete set of the eshelby tensors of an ellipsoidal inclusion,” *Journal of Applied Mechanics*, vol. 83, no. 12, p. 121010, 2016.
- [25] B. Torries, A. Imandoust, S. Beretta, S. Shao, and N. Shamsaei, “Overview on microstructure-and defect-sensitive fatigue modeling of additively manufactured materials,” *Jom*, vol. 70, no. 9, pp. 1853–1862, 2018.
- [26] K. Park and G. H. Paulino, “Cohesive zone models: a critical review of traction-separation relationships across fracture surfaces,” *Applied Mechanics Reviews*, vol. 64, no. 6, p. 060802, 2011.
- [27] Z.-H. Jin and C. Sun, “A comparison of cohesive zone modeling and classical fracture mechanics based on near tip stress field,” *Interna-*

- tional journal of solids and structures, vol. 43, no. 5, pp. 1047–1060, 2006.
- [28] F. Zhou and J.-F. Molinari, “Dynamic crack propagation with cohesive elements: a methodology to address mesh dependency,” *International Journal for Numerical Methods in Engineering*, vol. 59, no. 1, pp. 1–24, 2004.
- [29] C. Kuhn and R. Müller, “A continuum phase field model for fracture,” *Engineering Fracture Mechanics*, vol. 77, no. 18, pp. 3625–3634, 2010.
- [30] B. Bourdin, G. A. Francfort, and J.-J. Marigo, “The variational approach to fracture,” *Journal of elasticity*, vol. 91, no. 1-3, pp. 5–148, 2008.
- [31] G. Del Piero, “A variational approach to fracture and other inelastic phenomena,” *Journal of Elasticity*, vol. 112, no. 1, pp. 3–77, 2013.
- [32] S. Lee, M. F. Wheeler, and T. Wick, “Pressure and fluid-driven fracture propagation in porous media using an adaptive finite element phase field model,” *Computer Methods in Applied Mechanics and Engineering*, vol. 305, pp. 111–132, 2016.
- [33] B. A. Schrefler, S. Secchi, and L. Simoni, “On adaptive refinement techniques in multi-field problems including cohesive fracture,” *Computer methods in applied mechanics and engineering*, vol. 195, no. 4-6, pp. 444–461, 2006.
- [34] A. Khoei, H. Azadi, and H. Moslemi, “Modeling of crack propagation via an automatic adaptive mesh refinement based on modified superconvergent patch recovery technique,” *Engineering Fracture Mechanics*, vol. 75, no. 10, pp. 2921–2945, 2008.
- [35] H. Tada, P. Paris, and G. Irwin, “The analysis of cracks handbook,” *New York: ASME Press*, vol. 2, p. 1, 2000.
- [36] A. Lacazette, “Application of linear elastic fracture mechanics to the quantitative evaluation of fluid-inclusion decrepitation,” *Geology*, vol. 18, no. 8, pp. 782–785, 1990.
- [37] N. Moelans, B. Blanpain, and P. Wollants, “An introduction to phase-field modeling of microstructure evolution,” *Calphad*, vol. 32, no. 2, pp. 268–294, 2008.
- [38] N. Moelans, “A quantitative and thermodynamically consistent phase-field interpolation function for multi-phase systems,” *Acta Materialia*, vol. 59, no. 3, pp. 1077–1086, 2011.
- [39] N. Moelans, “A phase-field model for multi-component and multi-phase systems,” *Archives of Metallurgy and Materials*, vol. 53, no. 4, pp. 1149–1156, 2008.
- [40] J. M. G. Ribot, V. Agrawal, and B. S. Runnels, “A new approach for phase field modeling of grain boundaries with strongly nonconvex energy,” *Modelling and Simulation in Materials Science and Engineering*, 2019.
- [41] J. Towns, T. Cockerill, M. Dahan, I. Foster, K. Gaither, A. Grimshaw, V. Hazlewood, S. Lathrop, D. Lifka, G. D. Peterson, *et al.*, “Xsede: accelerating scientific discovery,” *Computing in Science & Engineering*, vol. 16, no. 5, pp. 62–74, 2014.

A. Coarse/fine stencil

It is instructive to find the equivalent numerical stencil corresponding to the reflux-free restriction operator. We begin with a one-dimensional example. Let $\phi_{f,4}$ be the fine node on the C/F boundary and $\phi_{c,2}$ be the coarse node on the C/F boundary as shown in Figure A.1. Let Δx_c and Δx_f be the spacings on the coarse and fine levels, respectively. The dashed lines indicate that the nodes are ghost nodes, and the “overlap” region is the coarse region over which the ghost nodes are located. As a simple yet representative example, let the field be single-component and let the differential operator be a

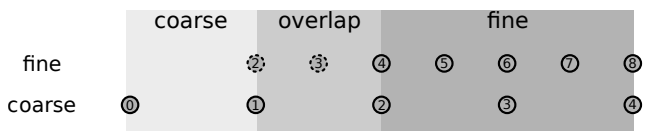


Figure A.1: 1D example of the grid at the C/F boundary

simple Laplacian:

$$D[\phi] = \frac{d^2\phi}{dx^2}. \quad (21)$$

Then, the operator acting on $\phi_{f,4}$ (i.e. the fine solution) is

$$D[\phi_{f,4}] = \frac{\phi_{f,5} - 2\phi_{f,4} + \phi_{f,3}}{\Delta x_f^2} \quad (22)$$

Since $\phi_{f,3}$ is restricted from the coarse level, then

$$\phi_{f,3} = \frac{1}{2}(\phi_{c,1} + \phi_{c,2}) = \frac{1}{2}(\phi_{c,1} + \phi_{f,4}). \quad (23)$$

Substituting (23) into (22) yields

$$D[\phi_{f,4}] = \frac{\phi_{f,5} - 2\phi_{f,4} + \frac{1}{2}(\phi_{c,1} + \phi_{f,4})}{\Delta x_f^2} \quad (24)$$

$$= \frac{\phi_{f,5} - \frac{3}{2}\phi_{f,4} + \frac{1}{2}\phi_{c,1}}{\Delta x_f^2}, \quad (25)$$

which may be alternatively written

$$D[\phi_{f,4}] = \frac{\phi_{f,5} - \phi_{f,4}}{\Delta x_f^2} - 2\frac{\phi_{c,2} - \phi_{c,1}}{\Delta x_c^2}, \quad (26)$$

corresponding to the Taylor series expansion of the operator at those points.

Now, let us revise to consider the effective stencil defined for a corner node in 2D. Let the operator be the Laplacian in 2D

$$D[\phi] = \frac{\partial^2\phi}{\partial x^2} + \frac{\partial^2\phi}{\partial y^2} \quad (27)$$

and let the stencil be defined as illustrated in Figure A.2. The operator acting at fine node $\phi_{f,4,4}$ is

$$D[\phi_{f,4,4}] = \frac{\phi_{f,5,4} - 2\phi_{f,4,4} + \phi_{f,3,4}}{\Delta x_f^2} + \frac{\phi_{f,4,5} - 2\phi_{f,4,4} + \phi_{f,4,3}}{\Delta y_f^2} \quad (28)$$

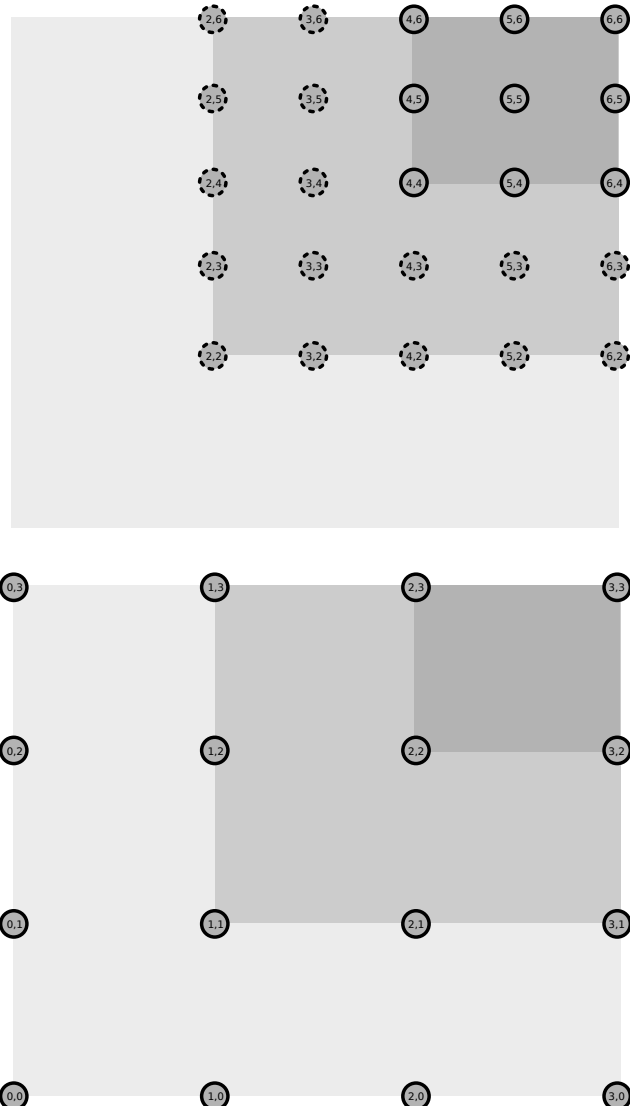


Figure A.2: Grid at a coarse/fine boundary for the fine grid (top) and coarse grid (bottom). The light gray region is coarse-only. The dark gray region is fine-only. The medium gray region is the overlap region over which the ghost nodes are defined.

Again realizing that $\phi_{f,4,3}$ and $\phi_{f,3,4}$ are restricted from the coarse grid, we have

$$\phi_{f,3,4} = \frac{1}{2}(\phi_{c,1,2} + \phi_{c,2,2}) \quad (29)$$

$$\phi_{f,4,3} = \frac{1}{2}(\phi_{c,2,1} + \phi_{c,2,2}). \quad (30)$$

Substituting (29) into (28) we have

$$D[\phi_{f,4,4}] = \frac{\phi_{f,5,4} - 2\phi_{f,4,4} + \frac{1}{2}(\phi_{c,1,2} + \phi_{c,2,2})}{\Delta x_f^2} +$$

$$\frac{\phi_{f,4,5} - 2\phi_{f,4,4} + \frac{1}{2}(\phi_{c,2,1} + \phi_{c,2,2})}{\Delta y_f^2}, \quad (31)$$

which can be written alternatively as either

$$D[\phi_{f,4,4}] = \frac{\phi_{f,5,4} - \frac{3}{2}\phi_{f,4,4} + \frac{1}{2}\phi_{c,1,2}}{\Delta x_f^2} + \frac{\phi_{f,4,5} - \frac{3}{2}\phi_{f,4,4} + \frac{1}{2}\phi_{c,2,1}}{\Delta y_f^2} \quad (32)$$

or

$$D[\phi_{f,4,4}] = \frac{\phi_{f,5,4} - \phi_{f,4,4}}{\Delta x_f^2} - 2\frac{\phi_{c,2,2} - \phi_{c,1,2}}{\Delta x_c^2} + \frac{\phi_{f,4,5} - \phi_{f,4,4}}{\Delta y_f^2} - 2\frac{\phi_{c,2,2} - \phi_{c,2,1}}{\Delta y_c^2}. \quad (33)$$

A similar procedure follows for other nodes along the coarse/fine boundary.